

# Micro Ring Resonator based CO<sub>2</sub> Gas Sensor using PbSe Quantum Dots

**Anvar Shahamat Hajikhanloo**

Islamic Azad University Mashhad Branch

**Mohammad Javadian Sarraf**

Islamic Azad University Mashhad Branch

**Ali Rostami** (✉ [rostami@tabrizu.ac.ir](mailto:rostami@tabrizu.ac.ir))

University of Tabriz <https://orcid.org/0000-0002-8727-4711>

**Mahboubeh Dolatyari**

University of Tabriz

---

## Research Article

**Keywords:** Micro-ring resonator (MRR), carbon dioxide (CO<sub>2</sub>) Sensor, PbSe, Quantum dot

**Posted Date:** July 6th, 2021

**DOI:** <https://doi.org/10.21203/rs.3.rs-638041/v1>

**License:** © ⓘ This work is licensed under a Creative Commons Attribution 4.0 International License.

[Read Full License](#)

---

# Micro Ring Resonator based CO<sub>2</sub> Gas Sensor using PbSe Quantum Dots

Anvar Shahamat Haji Khanloo<sup>1</sup>, Mohammad Javadian Sarraf<sup>1</sup>, Ali Rostami<sup>2,\*</sup>, Mahboubeh Dolatyari<sup>3</sup>

<sup>1</sup>Department of Electrical Engineering, Mashhad Branch, Islamic Azad University, Mashhad, Iran

<sup>2</sup>Photonics and Nanocrystal Research Laboratory, Faculty of Electrical and Computer Engineering, University of Tabriz, Tabriz 51664-16471, Iran

<sup>3</sup>SP-EPT Laboratories, ASEPE Company, Industrial Park of Advanced Technologies, Tabriz 53641-96795, Iran

[rostami@tabrizu.ac.ir](mailto:rostami@tabrizu.ac.ir)

**Abstract-** In this paper, we introduce a micro-ring resonator-based highly sensitive carbon dioxide sensor. For this purpose, a valley is created in the core of the ring and PbSe quantum dots (QDs) are deposited in the valley and the sensor is exposed to CO<sub>2</sub> gas. In this way, the refractive index of the PbSe QDs increases with an increase in the concentration of gas flow, and then the resonance frequency of the ring resonator shifts. The designed sensor operates almost linearly over a wide range of concentrations for CO<sub>2</sub> gas and shows a high resonance shift at different concentrations of CO<sub>2</sub> gas. The detection limit for the designed sensor is 0.001% of CO<sub>2</sub> gas which is more sensitive than previously reported sensors based on microring resonators. The frequency shifts are investigated by changing the width of the valley. The minimum width of the valley was determined for the evanescent field in which only the outer core of the ring affects the resonant frequency. Also, the modal analysis of the designed ring resonator waveguide is investigated to determine the minimum core width.

**Index Terms-** Micro-ring resonator (MRR), carbon dioxide (CO<sub>2</sub>) Sensor, PbSe, Quantum dot

## I. Introduction-

Various physical and chemical sensors have been introduced for detecting toxic, flammable, or explosive gases. Numerous gas sensors have been reported such as fluorescent, chemosensors [1-4], nondispersive infrared (NDIR) sensors [5], electrochemical sensors [6], thin films having porous silicon and mesoporous silica [7, 8], Raman spectroscopy [9], two-dimensional (2D) materials like Graphene [10] and acoustic gas sensors [1,11]. FET and MOSFET-based sensors have been reported by researchers for a long time. Kim and et al have reported a gas sensor based on MOSFET. They have used SnO<sub>x</sub> as a sensitive material to NO<sub>2</sub> gas which detection limit for the sensor is 50 ppm (0.005 %) [12]. In another MOSFET-based sensor has been reported by Hong [13] in which ZnO has been used as sensitive material to NO<sub>2</sub> and H<sub>2</sub>S gases with a detection limit of 0.002 %. This sensor is sensitive to CO<sub>2</sub>, CH<sub>4</sub>, SO<sub>2</sub>, NH<sub>3</sub>, and C<sub>3</sub>H<sub>8</sub>. However, sensitivity to these gases is low and the detection limit is 5%. Jeong and et al [14] investigate the gas sensing characteristics of the MOSFET-type sensor and WS<sub>2</sub> as the sensing layer. The presence of NO<sub>2</sub> gas increases the drain current of the sensor. However, the drain current decreases in the presence of H<sub>2</sub>S, and for other gases (NH<sub>3</sub> and CO<sub>2</sub>), the gas sensor has a small change of the drain current. Detection of ambient carbon dioxide has been investigated using Ti/Au layers deposited on the CaF<sub>2</sub> prism [15] with a quantum cascade (QCL) laser light excitation source. Also, the layer of ZnO/Au deposited on a flat surface of the prism [16] as a carbon dioxide sensor has also been investigated. Since precious metals such as gold and platinum are often used as sensitive materials in Plasmonic sensors, the cost of manufacturing these types of sensors is high.

Recently, the Hollow-core photonic crystal fibers (HC-PCFs) based Mach-Zehnder interferometer MZI method has been investigated for the detection and measurement of CO<sub>2</sub> [17]. There are three types of piezoelectric gas sensors: surface sound wave (SAW), quartz crystal microbalance (QCM) [18], and microelectromechanical systems (MEMS) [19, 20]. Various piezoelectric CO<sub>2</sub> gas sensors have been introduced [21, 22]. Piezoelectric sensors, including SAW and QCM, suffer from poor signal-to-noise performance [18] and environmental parameters such as temperature and humidity strongly interfere with their response. Photonic crystals also have been reported for sensing CO<sub>2</sub> gas. Photonic crystals (PhCs) have a periodic dielectric structure and the ability to guide and manipulating light in the range of optical wavelength. They have been studied extensively both in theory and experiment [23, 24]. The periodic arrangements of dielectric materials in PhCs produce a photonic bandgap (PBG) [25], and the propagation of light within the frequency range of PBG will be forbidden [26-29]. The main disadvantage of PhCs based sensors is the very precise control of the technological process during design and fabrication [25] but they are quite expensive [29] to fabricate. Several devices based on ring

resonators [30-33] have been reported. Ring resonators are promising candidates and have been widely used as sensors [34, 35]. They have good quality factors and enhancement of quality factors is possible for them [34]. For example, tandem-column micro-gas chromatography based on optofluidic ring resonators has been reported by Sun and coworkers [36]. An integrated Photonic gas sensor in coupled micro-ring resonators (MRRs) with a waveguide has been introduced by Zhou and others [37].

Ring resonators are photonic devices for selecting the resonance wavelength or resonance frequency and are excellent candidates for detecting gases, including CO<sub>2</sub> [38-40]. In most reported work, the principles of detection in MRR are based on the interaction of the evanescent field with ambient materials, including gas molecules, which change the refractive index of the effective propagation mode in the ring waveguide, which changes the wavelength or resonant frequency. Due to the rotation of light in MRR, the effective length of interaction with the gas-sensitive materials is longer and researchers usually deposit gas-sensitive materials on the ring resonator.

In this paper, we introduce a ring resonator-based optical carbon dioxide gas sensor using quantum dots; in which, PbSe quantum-dots (QDs) are used as sensitive material to CO<sub>2</sub> gas. For this purpose, PbSe QDs are deposited in the created valley in the core of the ring. As quantum dots have a high surface-to-volume ratio, so they can interact with more atoms of the target gas. The simplicity of the fabrication method and high sensitivity of the sensor are the advantages of these types of sensors. This sensor can easily detect gas in the concentration range of 0.001%-10%. According to our best knowledge, the best detection limit has been reported by Guangcan Mi et al which is 0.002% [38]; the detection limit for our designed sensor is less than 0.001%.

## II. THEORY AND MODELING

A basic micro ring resonator usually consists of one or two straight waveguides coupled to a circular ring. Fig. 1 shows a schematic of a micro-ring resonator consists of two straight waveguides and a single ring

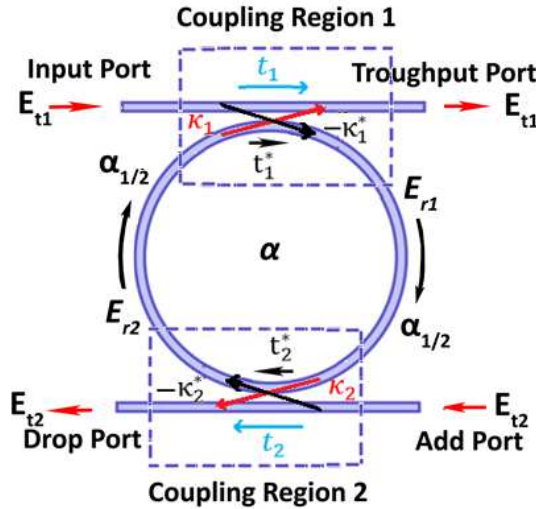


Fig. 1. Schematic of a single ring MRR with two straight waveguides.

Light is injected into the input port of MRR and the outputs of the system are taken from the throughput port of the upper waveguide and the drop port of the lower waveguide. We assumed  $E_{i1}$ ,  $E_{i2}$ ,  $E_{t1}$ , and  $E_{t2}$  as the electrical fields in input, add, throughput, and drop ports respectively.  $E_{r1}$  and  $E_{r2}$  are the half round trip field in the ring, on the right and left sides of the MRR respectively, which are propagated clockwise. According to Figure 1, MRR relationships can be described by a matrix relationship [41]:

$$\begin{bmatrix} E_{t1} \\ E_{t2} \\ E_{r1} \\ E_{r2} \end{bmatrix} = \begin{bmatrix} t_1 & 0 & 0 & \kappa_1 \alpha_{1/2} e^{j\theta_{1/2}} \\ 0 & t_2 & \kappa_2 \alpha_{1/2} e^{j\theta_{1/2}} & 0 \\ -\kappa_1^* & 0 & 0 & t_1^* \alpha_{1/2} e^{j\theta_{1/2}} \\ 0 & -\kappa_2^* & t_2^* \alpha_{1/2} e^{j\theta_{1/2}} & 0 \end{bmatrix} \begin{bmatrix} E_{i1} \\ E_{i2} \\ E_{r1} \\ E_{r2} \end{bmatrix} \quad (1)$$

where  $\alpha$  is the round trip loss coefficient [42] of the ring and  $\theta$  is the round trip phase [43],  $t_1$  and  $t_2$  are the self-coupling coefficients, also  $\kappa_1$  and  $\kappa_2$  are the cross-coupling coefficients [36]. In Eq. (1),  $\alpha_{1/2}$  and  $\theta_{1/2}$  are the half round trip loss and phase respectively, that  $\alpha_{1/2} = \sqrt{\alpha}$  and  $\theta_{1/2} = \frac{1}{2}\theta$ . The  $t_1^*$ ,  $t_2^*$ ,  $\kappa_1^*$  and  $\kappa_2^*$  denote the conjugated complex value of  $t_1$ ,  $t_2$ ,  $\kappa_1$  and  $\kappa_2$  respectively. By assuming no loss in the connections [42], the relation (2) will be obtained:

$$t^2 + \kappa^2 = 1 \quad (2)$$

Assuming  $E_{i1} = 1$  and  $E_{i2} = 0$  and using the matrix (1), the following relations will be obtained:

$$E_{r1} = \frac{-\kappa_1^*}{1-t_1^*t_2^*\alpha e^{j\theta}} \quad (3)$$

$$E_{r2} = \frac{-\kappa_1^*t_2^*\alpha_{1/2}e^{j\theta_{1/2}}}{1-t_1^*t_2^*\alpha e^{j\theta}} \quad (4)$$

$$E_{t1} = t_1 + \kappa_1 t_2^* \alpha e^{j\theta} E_{r1} = \frac{t_1 - t_1^* t_1^* t_2^* \alpha e^{j\theta} - \kappa_1^* \kappa_1 t_2^* \alpha e^{j\theta}}{1 - t_1^* t_2^* \alpha e^{j\theta}}$$

$$|t_1|^2 + |\kappa_1|^2 = 1 \Rightarrow E_{t1} = \frac{t_1 - t_2^* \alpha e^{j\theta}}{1 - t_1^* t_2^* \alpha e^{j\theta}} \quad (5)$$

$$E_{t2} = \frac{-\kappa_1^* \kappa_2 \alpha_{1/2} e^{j\theta_{1/2}}}{1 - t_1^* t_2^* \alpha e^{j\theta}} \quad (6)$$

Resonance wavelength of the ring resonator [44] ( $\lambda_{0,res}$ ) is given as follows:

$$\lambda_{0,res} = \frac{L}{m} n_{eff} = \frac{2\pi R}{m} n_{eff}, \quad (m = 1, 2, 3...) \quad (7)$$

where  $L$ ,  $n_{eff}$  and  $R$  are the length of the ring, the effective refractive index, and the radius of the ring respectively. The resonance wavelength shift ( $\Delta\lambda_{0,res}$ ) is obtained using Eq. (7):

$$|\Delta\lambda_{0,res}| = |\lambda_{0,res} - \lambda_{0,res1}| = \frac{2\pi R}{m} |n_{eff} - n_{eff1}| = \frac{2\pi R}{m} |\Delta n_{eff}| \quad (8)$$

where  $\lambda_{0,res1}$ ,  $n_{eff1}$  and  $\Delta n_{eff}$  are the resonance wavelength after interaction with gas, the effective refractive index of the ring after interaction with gas, and change the effective refractive index respectively. By dividing Eq. (8) to Eq. (7), the relative resonance wavelength shift is obtained as follows:

$$\frac{|\Delta\lambda_{0,res}|}{\lambda_{0,res}} = \frac{|\Delta n_{eff}|}{n_{eff}} \quad (9)$$

The resonant frequency is obtained from the relation of angular frequency [41]  $\omega = kc$  and the relation between wavelength  $\lambda$  and wavenumber  $k = 2\pi / \lambda$  and relation (7):

$$f_{0,res} = \frac{mc}{2\pi R n_{eff}} \quad (10)$$

where  $f_{0,res}$  and  $c$  is the resonance frequency of the ring and speed of light in a vacuum respectively. The resonance frequency shift ( $\Delta f_{0,res}$ ) is obtained using Equation (10):

$$|\Delta f_{0,res}| = |f_{0,res} - f_{0,res1}| = \left| \frac{mc}{2\pi R n_{eff}} - \frac{mc}{2\pi R n_{eff1}} \right| = \left| \frac{mc(n_{eff1} - n_{eff})}{2\pi R n_{eff} n_{eff1}} \right| \quad (11)$$

Where  $f_{0,res1}$  is the resonance frequency of the ring after interaction with gas. By dividing Eq. (11) to Eq. (10), the relative resonance frequency shift is obtained:

$$\frac{|\Delta f_{0,res}|}{f_{0,res}} = \frac{|\Delta n_{eff}|}{n_{eff1}} \quad (12)$$

At low gas concentrations, the difference between  $n_{eff}$  and  $n_{eff1}$  is negligible, which will give:

$$\frac{|\Delta f_{0,res}|}{f_{0,res}} \approx \frac{|\Delta\lambda_{0,res}|}{\lambda_{0,res}} = \frac{|\Delta n_{eff}|}{n_{eff}} \quad (13)$$

In this work, we designed a micro-ring resonator (MRR) based CO<sub>2</sub> gas sensor that used the PbSe quantum dots deposited in the created valley in the middle core of the ring as a carbon dioxide-sensitive material. 2D simulations have been performed in the wave optics module of COMSOL Multiphysics software. The 2D configuration of the micro ring resonator-based CO<sub>2</sub> gas sensor is shown in Fig. 2a and its 3D configuration is shown in Fig. 2b. This study is set up using the electromagnetic Waves, Beam Envelopes interface, and a field continuity boundary condition is used at the boundary between the straight waveguide and the ring waveguide. Also, the scattering boundary conditions are used at the boundary between MRR and the environment. The configuration dimensions were obtained using simulation results at a resonant frequency of 193.41 [THz] (1.55 $\mu$ m) without the presence of CO<sub>2</sub> gas. The width, height, and length of the straight waveguide clad were

selected as  $3\mu\text{m}$ ,  $1.5\mu\text{m}$ , and  $18.8488\mu\text{m}$  respectively. The width and height of the straight waveguide were selected to be  $0.35\mu\text{m}$ . The radius of the ring (from the center of the ring to the middle of the valley) is  $6.9244\mu\text{m}$ , the height and width of the ring cores were selected  $0.35\mu\text{m}$  and the width of the valley was selected  $2\mu\text{m}$ . We chose the width and height of the ring clad  $5\mu\text{m}$  and  $1.5\mu\text{m}$  respectively. The distance from the straight waveguide core and the outer ring core (gap) is  $0.12\mu\text{m}$ .

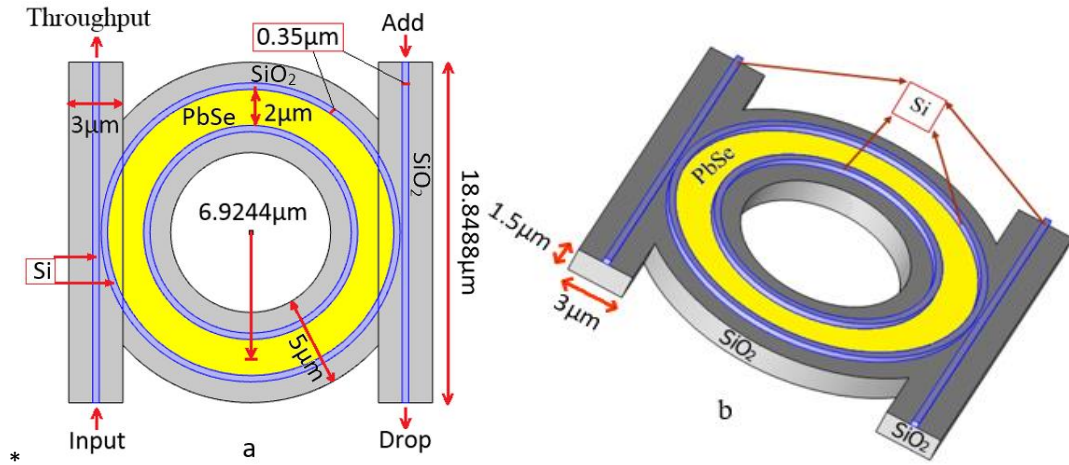


Fig. 2. The ring resonator-based CO<sub>2</sub> gas sensor configuration (a) 2D and (b) 3D

In this work, the clad material is SiO<sub>2</sub> and the core material of the micro ring resonator is silicon. The refractive index of Si at room temperature at  $1.55\mu\text{m}$  wavelength is 3.4757 [45]. The clad refractive index of SiO<sub>2</sub> at room temperature for wavelength  $1.55\mu\text{m}$  is 1.444 [46]. The optical properties of the quantum dot (PbSe) with the size of  $1.5\text{nm}$  with and without the presence of CO<sub>2</sub> gas were calculated by the density-functional theory (DFT) method. The calculated refractive index for bare QDs and PbSe bonded with oxygen atoms of CO<sub>2</sub> gas is shown in Fig. 3 and 4. As the figures show, the refractive index increases with absorbing the CO<sub>2</sub> gas. There are dangling bonds on the surface of the nano-crystal before absorbing CO<sub>2</sub>. Bonding of surface atoms with CO<sub>2</sub> molecules decreases dangling bonds and this decreases free carries in the crystal which leads to an increase in refractive index.

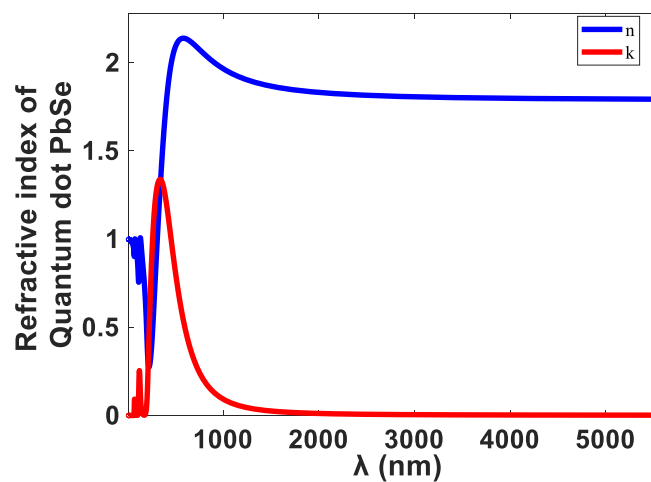


Fig. 3. The refractive index of quantum dot PbSe with size  $1.5\mu\text{m}$

Using the Lorentz-Lorenz model [47, 48] for the refractive index of composite materials, the effective refractive index of PbSe quantum dots after interaction with the CO<sub>2</sub> will be:

$$\left(\frac{n_e^2-1}{n_e^2+2}\right) = (1-p) \left(\frac{n_c^2-1}{n_c^2+2}\right) + p \left(\frac{n_d^2-1}{n_d^2+2}\right) \quad (14)$$

where  $p$  is the percentage of CO<sub>2</sub> gas,  $n_e$ ,  $n_c$  and  $n_d$  are the effective refractive index, the refractive index of PbSe quantum dots, and the refractive index of PbSe-CO<sub>2</sub> respectively.

**Density Functional Theory (DFT) Calculations-** The electronic band structure along with the optical properties of PbSe, PbSe-CO<sub>2</sub> quantum dots were calculated using the DFT algorithm with the CASTEP code [49] and optimized using the BFGS (Broyden-Fletcher-Goldfarb-Shanno) geometry optimization method [49]. Generalized gradient approximation (GGA) and the non-local gradient-corrected exchange-correlation functional as parameterized by Perdew-Burke-Ernzerhof (PBE) used in the calculation which uses a plane wave basis set for the valence electrons and norm-conserving pseudopotential (NCP) [50, 51] for the core electrons. The number of plane waves included in the basis was determined from the cut-off energy ( $E_c$ ) of 500.0 eV. The summation over the Brillouin zone was carried out with  $k$  point sampling using a Monkhorst-Pack grid with parameters of  $2 \times 2 \times 2$ . Geometry optimization under applied hydrostatic pressure can be used to determine the modulus of a material ( $B$ ) and its pressure derivative,  $B' = dB/dP$ .

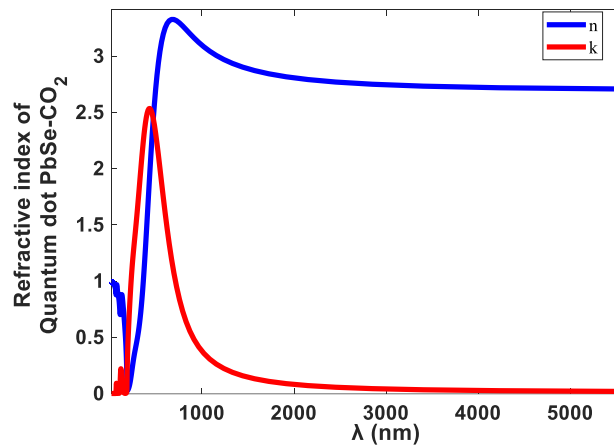


Fig. 4. The refractive index of the PbSe-CO<sub>2</sub> quantum dot

**II. Simulation and Discussion-** To analyze a micro-ring resonator-based CO<sub>2</sub> gas sensor, its dimensions must be determined before any action at the reference resonance frequency without the presence of the gas to electromagnetic waves propagate inside the straight waveguide core and coupled to the ring core. In this work, the reference frequency is 193.41 [THz] (1.55 $\mu$ m) and a modal analysis of the straight waveguide core is performed. According to the number of propagating modes in a straight waveguide core, its dimensions were determined. The dimensions of the ring core are equal to the dimensions of the straight waveguide core. The cross-sectional view of the straight waveguide is shown in Figure 5 and its modal analysis in terms of the width of the waveguide core is shown in Figure 6. The width of the core in the straight waveguide is equal to its height. According to the curve in Fig. 6, if the width of the core is less than 0.25 $\mu$ m, no mode can fully propagate in the core. For the width of the core in the range 0.27 $\mu$ m to 0.361 $\mu$ m, we will have two modes that can be fully propagated in the core which is clearly shown in Fig. 7a to 7f for a core width of 0.34516 $\mu$ m. In this work, the core width is 0.35 $\mu$ m.

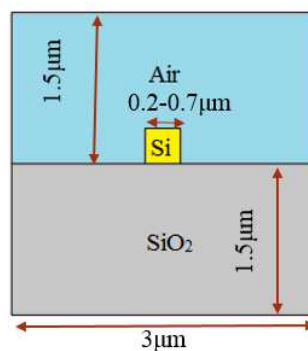


Fig. 5. Cross-section view of the straight waveguide.

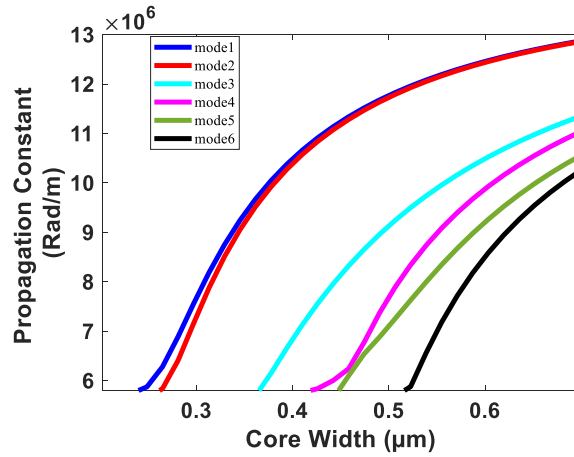


Fig. 6. The propagation constant according to the width of the core in the straight waveguide in the first 6 modes at  $f_0=193.41$ [THz].

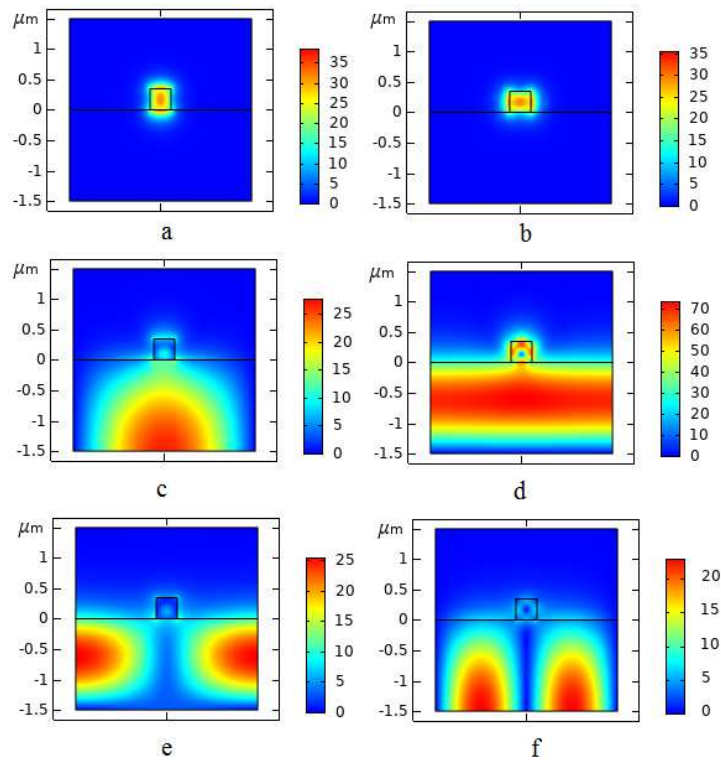


Fig. 7. Electric field norm (V/m) in core width  $0.34516\mu\text{m}$  with effective mode index a) 2.2805 b) 2.2337 c) 1.4034 d) 1.3754 e) 1.3512 f) 1.328.

When the core width is greater than  $0.523\mu\text{m}$ , all 6 modes are propagated completely in the core. For full propagation of all 6 modes, we have shown the profile of the electric field norm for the core width of  $0.7\mu\text{m}$  according to Fig. 8. To determine the radius of the ring at the reference frequency ( $193.41$  [THz]), by simulating the proposed design concerning the parameter  $r_0$  (ring radius) (according to Fig. 9) a resonance is observed in the radius  $r_0 = 6.8458\mu\text{m}$  and the radius  $r_0 = 6.9244\mu\text{m}$ . Also, Fig. 9 shows energy savings. The profile of the electric field norm in the resonance radius ( $r_0 = 6.9244\mu\text{m}$ ) in valley width (VW) of  $2\mu\text{m}$  is shown in Fig. 10. To analyze the frequency response in the designed sensor, the radius  $r_0 = 6.9244\mu\text{m}$  for the MRR was applied.

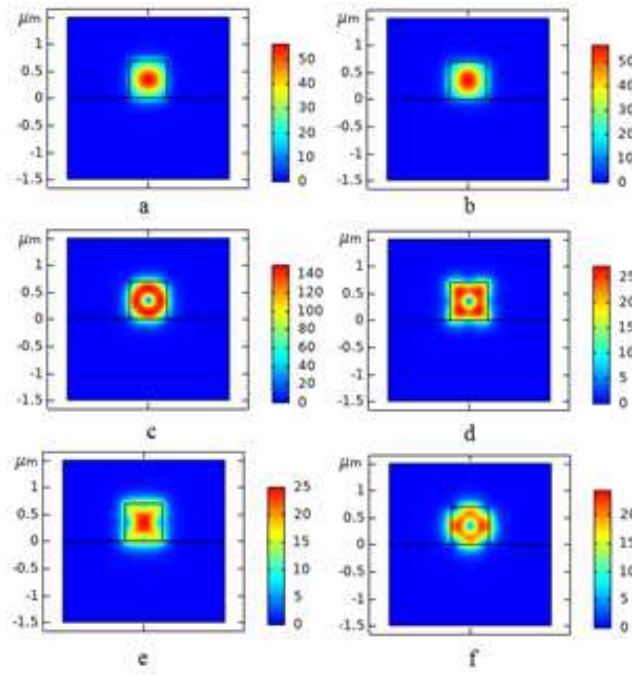


Fig. 8. Electric field norm (V/m) in core width  $0.7\mu\text{m}$  with effective mode index a) 3.1758 b) 3.1731 c) 2.8009 d) 2.7237 e) 2.6053 f) 2.5307.

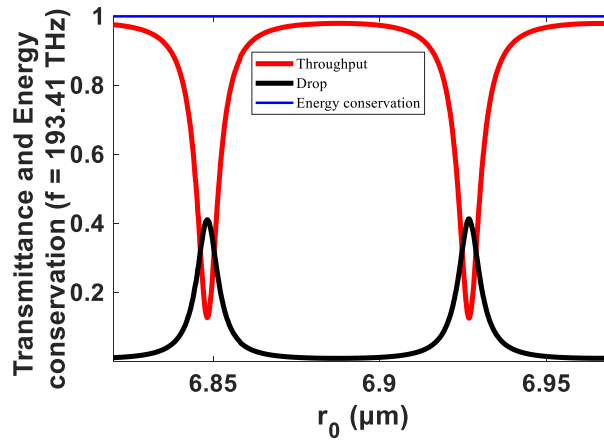


Fig. 9. Transmittance and energy conservation to the ring radius at the frequency ( $f_0 = 193.41[\text{THz}]$ ).

$$(r_{0_{res1}} = 6.8482 \mu\text{m}, r_{0_{res2}} = 6.9244 \mu\text{m})$$

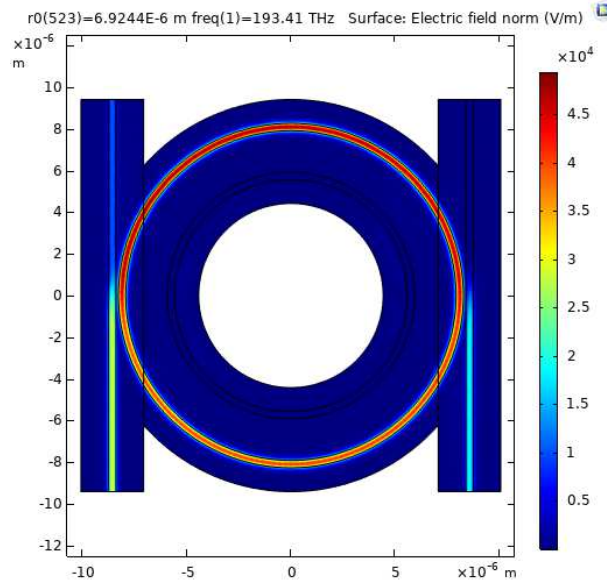


Fig. 10. Electric field norm for resonance radius ( $r_0 = 6.9244\mu\text{m}$  at frequency ( $f_0 = 193.41[\text{THz}]$ ) in (valley width =  $2\mu\text{m}$ ).

The resonant light has an evanescent field of about a few hundred nanometers that penetrate around the core of the ring. If the evanescent field of the outer core penetrates the inner core, changes in  $\text{CO}_2$  concentration cause to create two resonance radius (RR) or  $r_{0\text{res}}$ , one for the outer core and another for the inner core of the ring. In the valley widths of  $0.05\mu\text{m}$ ,  $0.1\mu\text{m}$ , and  $0.15\mu\text{m}$ , in addition to the resonant radius in the outer core of the ring, there is another resonant radius for the inner core of the ring. There will be two resonance radius per  $\text{CO}_2$  concentration (see Fig. 11), which will result in two resonant frequencies. To avoid creating two resonance radius, the width of the valley should not be less than the penetration depth of the evanescent field. As shown in Fig.11, for valley width of  $0.2\mu\text{m}$ , there is only one resonant frequency for the ring core. Fig. 12 shows the norm electric field, which indicates the resonant radius for the outer and inner cores of the ring within the valley width of  $0.1\mu\text{m}$ .

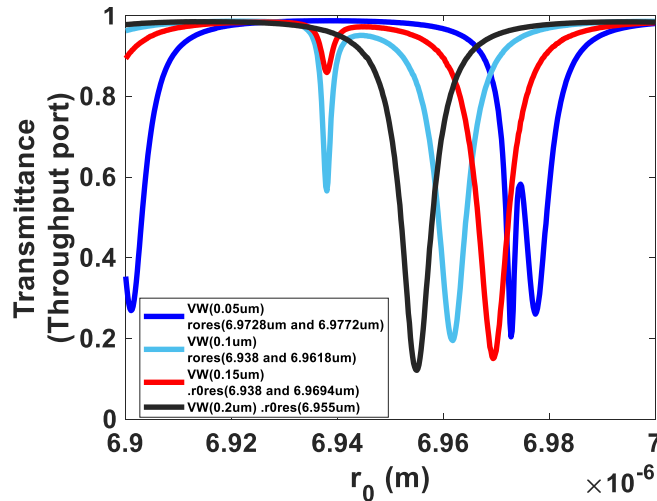


Fig. 11. Transmittance according to the ring radius for the valley width (VW) of  $0.05\mu\text{m}$ ,  $0.1\mu\text{m}$ ,  $0.15\mu\text{m}$ , and  $0.2\mu\text{m}$  at frequency  $193.41[\text{THz}]$  (Throughput port).

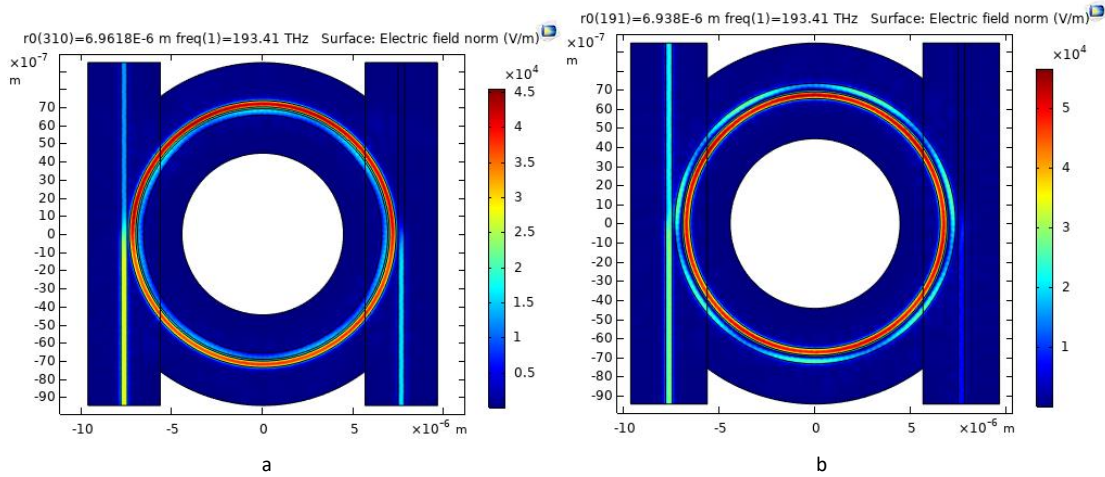


Figure 12. Electric field norm at frequency 193.41 [THz] for the valley width  $0.1\mu\text{m}$  with a) resonance radius in the outer core of the ring equal to  $6.9618\mu\text{m}$  and b) resonance radius in the inner core of the ring equal to  $6.938\mu\text{m}$ .

To have enough space to deposit the PbSe quantum dots into the valley and also to have only one resonant frequency for the outer core of the ring, we selected the valley width of  $2\mu\text{m}$  and simulated the transmittance and frequency response at different  $\text{CO}_2$  concentrations.

The resonance frequency at different  $\text{CO}_2$  concentrations in the drop port is shown in Fig. 13. Also, Fig. 14 shows the resonance frequency at different  $\text{CO}_2$  concentrations in the throughput port. The  $\text{CO}_2$  concentration swiped from 0% to 10%. The results indicate that for per 1% change at  $\text{CO}_2$  concentration, the shift at the resonant frequency of the sensor approximately linearly changes (see Fig. 15). Increasing per 1%  $\text{CO}_2$  concentration shows approximately 8803 MHz shift at resonant frequency (as shown in Fig. 13 and Fig. 14) which indicates the high sensitivity of the designed sensor. A frequency shift of about 0.5 MHz occurs at 0.001%  $\text{CO}_2$  concentration. On the other hand, due to the increase of the imaginary part of the effective refractive index to the increasing  $\text{CO}_2$  concentration, the amplitude of the electric field will decrease with increasing  $\text{CO}_2$  concentration.

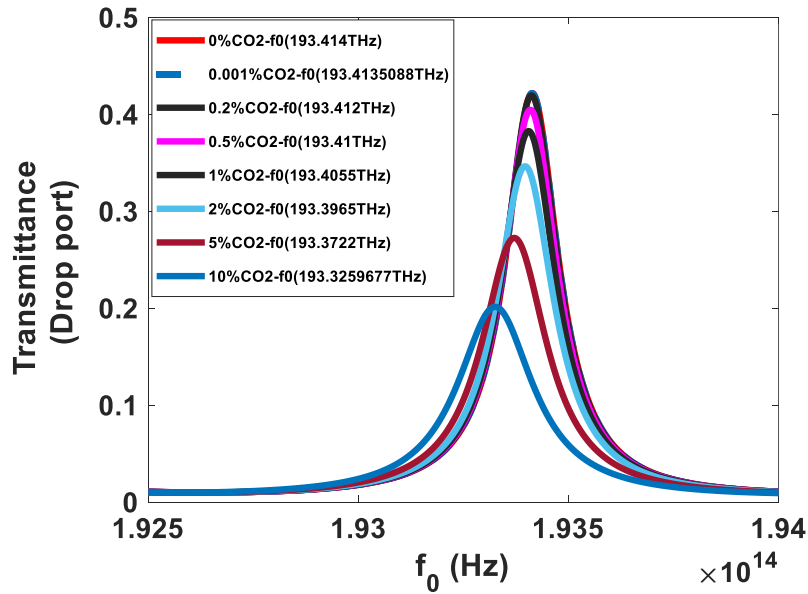


Fig. 13. Transmittance at different  $\text{CO}_2$  concentrations for the valley width of  $2\mu\text{m}$  (Drop port)

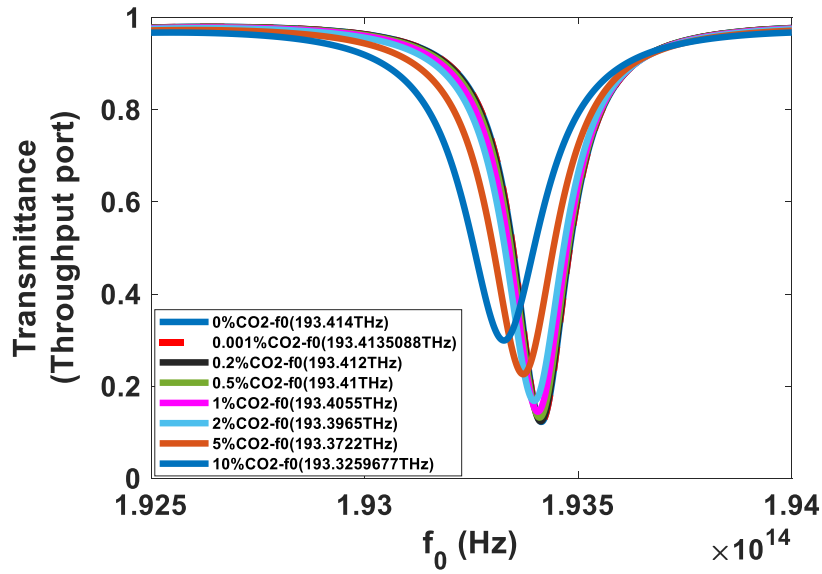


Fig. 14. Transmittance at different CO<sub>2</sub> concentrations for the valley width of 2 μm (Throughput port).

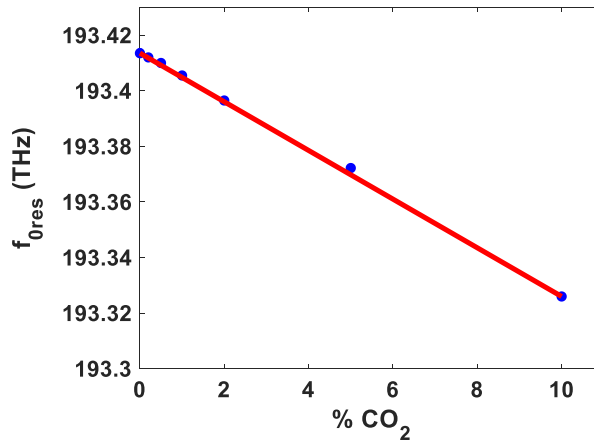


Fig. 15. Resonance frequencies at different CO<sub>2</sub> concentrations (valley width = 2 μm).

We also simulated the performance of the sensor for the valley width of 0.2 μm at CO<sub>2</sub> similar concentrations with the valley width of 2 μm. As shown in Fig. 16, we can reach a more resonance frequency shift at similar CO<sub>2</sub> concentrations for the valley width of 0.2 μm. With increasing the CO<sub>2</sub> concentrations from 0 to 10 % resonance frequency decreases. As fig 17 shows the resonance frequency linearly decreases with increasing CO<sub>2</sub> concentration.

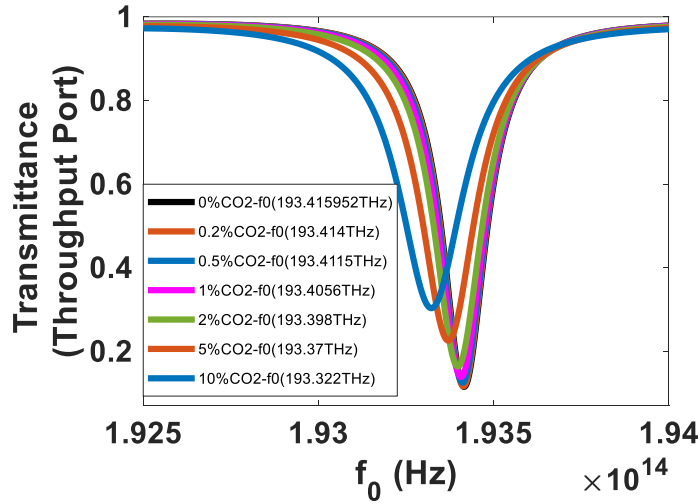


Fig. 16. Transmittance at different CO<sub>2</sub> concentrations for the valley width of 0.2  $\mu\text{m}$  (Throughput port).

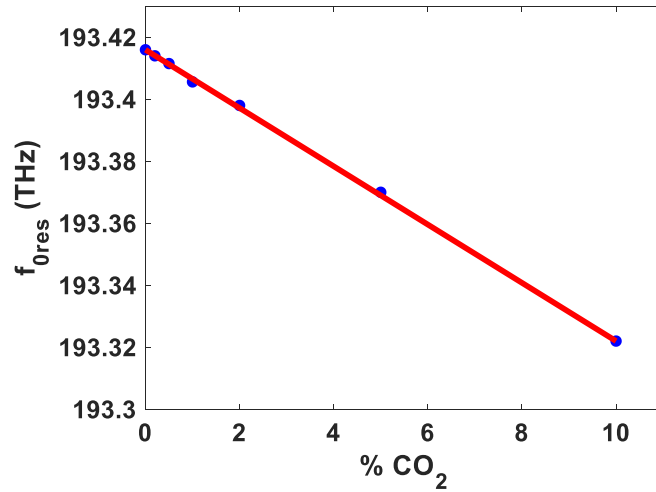


Fig. 17. Resonance frequencies at different CO<sub>2</sub> concentrations (valley width = 0.2  $\mu\text{m}$ ).

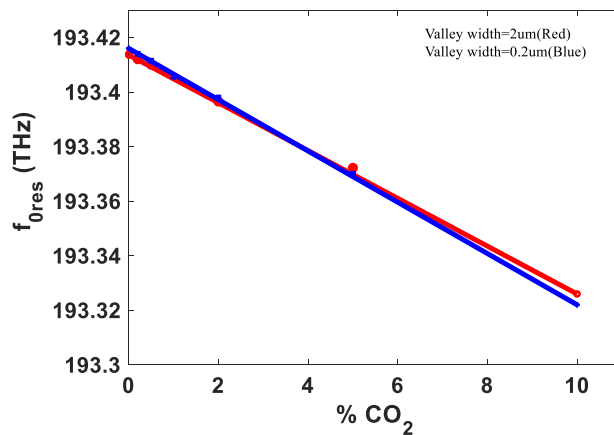


Figure 18. Comparison of resonance frequencies at different CO<sub>2</sub> concentrations for the valley width of 2  $\mu\text{m}$  (red) and 0.2  $\mu\text{m}$  (blue).

The resonance frequency for the valley width of 0.2  $\mu\text{m}$  at similar concentrations of CO<sub>2</sub> gas has a higher slope compared to the valley width of 2  $\mu\text{m}$  as shown in Fig. 18.

For the valley widths of 0.2  $\mu\text{m}$  and 2  $\mu\text{m}$ , the resonance frequency shift at different CO<sub>2</sub> concentrations from 0% to 10% is almost linear. For the valley widths of 0.2  $\mu\text{m}$  and 2  $\mu\text{m}$ , the resonance frequencies shifts at 0.05%

CO<sub>2</sub> concentration are 0.5176 GHz (4.15 pm) and 0.425 GHz (3.41 pm) respectively, which the relative resonance frequency shifts will be  $2.676 \times 10^{-6}$  and  $2.197 \times 10^{-6}$ , as shown in Table 1. These results indicate more sensitivity of our designed sensor rather than previously reported research works. In the work reported by Guangcan Mi et al [35], for CO<sub>2</sub> concentrations from 0.005% to 0.05%, the sensor wavelength shift is almost linear too. For the reference wavelength of 1550 nm and 0.05% CO<sub>2</sub> gas concentration, the resonance wavelength shift is 2 pm, which gives a relative resonance wavelength shift  $1.29 \times 10^{-6}$ . Also in another work reported by Karanam Pallavi Koushik et al [37], at CO<sub>2</sub> concentrations from 0.005% to 0.05%, the sensor wavelength shift is almost linear and the resonance wavelength shift at 0.05% CO<sub>2</sub> concentration is 1.82 pm, which gives a relative resonance wavelength shift  $1.17 \times 10^{-6}$ .

Table 1. Resonance frequency shift or resonance wavelength shift and relative resonance frequency shift or relative resonance wavelength shift (proportional to sensitivity) at 0.05% CO<sub>2</sub> gas concentration.

Results and calculations using	$\lambda_{0,res} [nm]$	$f_{0,res} [THz]$	$\Delta\lambda_{0,res} [pm]$	$\Delta f_{0,res} [GHz]$	$\frac{ \Delta f_{0,res} }{f_{0,res}} \approx \frac{ \Delta\lambda_{0,res} }{\lambda_{0,res}}$
Ref. [35]	1550.000	193.548	2	0.2497	$1.29 \times 10^{-6}$
Ref. [37]	1550.000	193.548	1.82	0.2273	$1.17 \times 10^{-6}$
Our work in valley with=0.2 $\mu$ m	1551.065	193.415952	4.1508	0.5176	$2.676 \times 10^{-6}$
Our work in valley with=2 $\mu$ m	1551.077	193.414	3.4082	0.425	$2.197 \times 10^{-6}$

## V. CONCLUSION

We have described a micro ring resonator-based carbon dioxide sensor using the PbSe quantum dots. This sensor is very sensitive to changes in CO<sub>2</sub> concentration and its detection limit is 0.001 %. Also, due to the 9 GHz resonant frequency shift per 1% CO<sub>2</sub> concentration, it can be measured and tested with conventional spectrum analyzer systems. This sensor due to the higher resonance shift has more sensitivity than the previous MRR-based optical CO<sub>2</sub> sensors. We also investigated the effect of valley width on the sensitivity of PbSe to sensing CO<sub>2</sub> gas. Also, the minimum dimensions for valley width to have a resonant frequency only in the outer core were determined.

## REFERENCES

- [1] A. Cicek, D. Trak, Y. Arslan, N. Korozlu, O. A. Kaya, and B. Ulug, "Ultrasonic gas sensing by two-dimensional surface phononic crystal ring resonators", *ACS Sens.*, Vol. 4, No. 7, pp. 1761–1765 (2019).
- [2] Z. Guo, N. R. Song, J. H. Moon, M. Kim, E. J. Jun, J. Choi, J. Y. Lee, C. W. Bielawski, J. L. Sessler, and J. Yoon, "A benzobisimidazolium-based fluorescent and colorimetric chemosensor for CO<sub>2</sub>", *J. Am. Chem. Soc.*, Vol. 134, No.43, pp. 17846–17849 (2012).
- [3] Y. Liu, Y. Tang, N. N. Barashkov, I. S. Irgibaeva, J. W. Y. Lam, R. Hu, D. Birimzhanova, Y. Yu and B. Z. Tang, "Fluorescent chemosensor for detection and quantitation of carbon dioxide gas", *J. Am. Chem. Soc.*, Vol. 132, No.40, pp. 13951–13953 (2010).
- [4] Q. Xu, S. Lee, Y. Cho, M. H. Kim, J. Bouffard, and J. Yoon, "Polydiacetylene-based colorimetric and fluorescent chemosensor for the detection of carbon dioxide", *J. Am. Chem. Soc.*, Vol. 135, No.47, pp. 17751–17754 (2013).
- [5] J. Zosel, W. Oelßner, M. Decker, G. Gerlach, and U. Guth, "The measurement of dissolved and gaseous carbon dioxide concentration", *Meas. Sci. Technol.*, 22, No. 7, 072001 (2011).
- [6] J. J. Gassensmith, J. Y. Kim, J. M. Holcroft, O. K. Farha, J. F. Stoddart, J. T. Hupp, and N. C. Jeong, "A metal-organic framework-based material for electrochemical sensing of carbon dioxide", *J. Am. Chem. Soc.*, Vol. 136, No. 23, pp. 8277–8282 (2014).
- [7] T. V. K. Karthik, L. Martinez and V. Agarwal, "Porous silicon ZnO/SnO<sub>2</sub> structures for CO<sub>2</sub> detection", *J. Alloys Compd.*, Vol. 731, pp. 853– 863 (2018).
- [8] H. J. Lee, K. K. Park, M. Kupnik, N. A. Melosh, and B. T. Khuri-Yakub, "Mesoporous thin-film on the highly-sensitive resonant chemical sensor for relative humidity and CO<sub>2</sub> detection", *Anal. Chem.*, Vol. 84, No. 7, pp. 3063-3066 (2012).
- [9] D. V. Petrov, I. I. Matrosov and A. R. Zaripov, "Determination of atmospheric carbon dioxide concentration using Raman spectroscopy", *J. Mol. Spectrosc.* Vol. 348, pp. 137–141 (2018).
- [10] S. J. Kim, H. J. Koh, C. E. Ren, O. Kwon, K. Maleski, S. Y. Cho, B. Anasori, C. Kim, Y. Choi, J. Kim, Y. Gogotsi and H. T. Jung, "Metallic Ti<sub>3</sub>C<sub>2</sub>T<sub>x</sub> MXene gas sensors with ultrahigh signal-to-noise ratio", *ACS Nano*, Vol. 12, No.2 pp. 986–993 (2018).
- [11] M. A. Butt, S. N. Khonina and N. L. Kazanskiy, "metal-insulator-metal nano square ring resonator for gas sensing applications", *Waves in Random and Complex Media*, Vol. 31, No. 1, pp. 146-156 (2019).
- [12] C.H. Kim, In-Tak Cho, Jong-Min Shin, Kyu-Bong Choi, Jung-Kyu Lee, and Jong-Ho Lee, "A New Gas Sensor Based on MOSFET Having a Horizontal Floating-Gate", *IEEE Electr. Device Lett.*, VOL. 35, NO. 2, (2014).

- [13] Y. Hong a , C.H. Kima , J. Shin, K.Y. Kimb , J.S. Kimc , C.S. Hwang and J.H. Lee, "Highly selective ZnO gas sensor based on MOSFET having a horizontal floating-gate", *Sens. Act. B: Chem.*, Vol. 232, pp. 653-659 (2016).
- [14] Y. Jeonga, J. Shina, Y. Honga, M. Wua, S. Honga, K.C. Kwonb, S. Choib, T. Leeb, H.W. Jangb and J.H. Lee, "Gas sensing characteristics of the FET-type gas sensor having inkjet-printed WS<sub>2</sub> sensing layer", *Solid State Electronics*, Vol. 153, pp. 27-32, (2019).
- [15] S. Herminjard, L. Sirigu, H. P. Herzig, E. Studemann, A. Crottini, J. P. Pellaux, T. Gresch, M. Fischer and J. Faist, "Surface plasmon resonance sensor showing enhanced sensitivity for CO<sub>2</sub> detection in the mid-infrared range", *Optics Express*, Vol. 17, No. 1 , pp. 293-303, (2009).
- [16] R. Nuryadi, and R. D. Mayasari, "ZnO/Au-based surface plasmon resonance for CO<sub>2</sub> gas sensing application", *Applied Physics A.*, Vol. 122, No. 1 pp. 33, (2016).
- [17] F. Ahmed, V. Ahsani, K. Nazeri, E. Marzband, C. Bradley, E. Toyserkani, and M. B. Jun, "Monitoring of Carbon Dioxide Using Hollow-Core Photonic Crystal Fiber Mach-Zehnder Interferometer", *Sensors*, Vol. 19, No. 15, pp. 3357, (2019).
- [18] K. Arshak, E. Moore, G. M. Lyons, J. Harris, and S. Clifford, "A review of gas sensors employed in electronic nose applications", *Sensor Review*, Vol. 24, pp. 181-198, (2004).
- [19] S. Tadigadapa and K. Mateti, "Piezoelectric MEMS sensors: state-of-the-art and perspectives", *Measurement Science and Technology*, Vol. 20, pp. 092001, (2009).
- [20] Y. Javed, M. Mansoor, and I. A. Shah, "A review of principles of MEMS pressure sensing with its aerospace applications", *Sensor Review*, (2019).
- [21] M. T. Gomes, A. C. Duarte and J. P. Oliveira, "Detection of CO<sub>2</sub> using a quartz crystal microbalance", *Sensors and Actuators B: Chemical*, Vol. 26, No. 1-3, pp. 191-194, 1995.
- [22] M. Berouaken, L. Talbi, R. Alkama, S. Sam, H. Menari, K. Chebout, A. Manseri, A. Boucheham, and N. Gabouze, "Quartz Crystal Microbalance Coated with Vanadium Oxide Thin Film for CO<sub>2</sub> Gas Sensor at Room Temperature", *Arabian Journal for Science and Engineering*, Vol. 43, No. 11, pp. 5957-5963, (2018).
- [23] A. Scherer, O. Painter, J. Vuckovic, M. Loncar, and T. Yoshie, "Photonic crystals for confining, guiding, and emitting light", *IEEE transactions on nanotechnology*, Vol. 1, No. 1, pp. 4-11 (2002).
- [24] J. D. Joannopoulos, P. R. Villeneuve and S. Fan, "Photonic crystals: putting a new twist on the light", *Nature*, Vol. 386, No. 6621, pp. 143-149, (1997).
- [25] H. Xu, P. Wu, C. Zhu, A. Elbaz and Z. Z. Gu, "Photonic crystal for gas sensing", *Journal of Materials Chemistry C.*, Vol. 1, No. 38, pp. 6087-6098, (2013).
- [26] J. D. Joannopoulos, S. G. Johnson, J. N. Winn, and R. D. Meade, "Molding the flow of light", Princeton Univ. Press, Princeton, NJ [ua], (2008).
- [27] B. Troia, A. Paolicelli, F. De Leonardis, and V. M. Passaro, "Photonic crystals for optical sensing: A review", *Advances in Photonic Crystals*, pp. 241-295, (2013).
- [28] D. Pergande, T. M. Geppert, A. V. Rhein, S. L. Schweizer, R. B. Wehrspohn, S. Moretton and A. Lambrecht, "Miniature infrared gas sensors using photonic crystals", *Journal of Applied Physics*, Vol. 109, No. 8, pp. 083117, (2011).
- [29] Y. Zhao, Y. N. Zhang, and Q. Wang, "Research advance of photonic crystal gas and liquid sensors", *Sensors and Actuators B: Chemical*, Vol. 160, No. 1, pp. 1288-1297, (2011).
- [30] S. Xiao, L. Liu, and M. Qiu, "Resonator channel drop filters in a plasmon-polaritons metal", *Opt Express*, Vol. 14, No. 7, pp. 2932-2937 (2006).
- [31] M. A. Butt, S. N. Khonina and N. L. Kazanskiy, "Hybrid plasmonic waveguide-assisted metal-insulator-metal ring resonator for refractive index sensing", *J Mod Optics*, Vol. 65, No. 9, pp.1135-1140 (2018).
- [32] M. A. Butt, S. N. Khonina and N. L. Kazanskiy, "Highly sensitive refractive index sensor based on hybrid plasmonic waveguide microring resonator", *Waves in Random and complex media*, Vol. 30, No. 2, pp. 292-299 (2020).
- [33] Z. Zhang, J. Yang, X. He, J. Zhang, J. Huang, D. Chen, and Y. Han, "Plasmonic refractive index sensor with high figure of merit based on concentric-rings resonator", *Sensors*, Vol. 18, No. 116, pp. 1-14(2018).
- [34] M. H. Zarifi and M. Daneshmand, "Wide dynamic range microwave planar coupled ring resonator for sensing applications", *Appl. Phys. Lett.*, Vol. 108, No. 23, 232906 (2016).
- [35] M. H. Zarifi, M. Rahimi, M. Daneshmand and T. Thundat, "Microwave ring resonator-based non-contact interface sensor for oil sands applications", *Sens. Actuators, B*, Vol. 224, pp. 632-639 (2016).
- [36] Y. Sun, J. Liu, D. J. Howard, G. Frye-Mason, A. K. Thompson, S. J. Ja, and X. Fan, "Rapid tandem-column micro-gas chromatography based on optofluidic ring resonators with multi-point on-column detection", *Analyst*, Vol. 135, No. 1, pp. 165-171 (2010).
- [37] X. Zhou, L. Zhang, A. M. Armani, J. Liu, X. Duan, D. Zhang, H. Zhang and W. Pang, "An integrated photonic gas sensor enhanced by optimized Fano effects in coupled microring resonators with an athermal waveguide", *Journal of Lightwave Technology*, Vol. 33, No. 22, pp. 4521-4530 (2015).
- [38] G. Mi, C. Horvath, M. Aktary and V. Van, "Silicon microring refractometric sensor for atmospheric CO<sub>2</sub> gas monitoring", *Optics Express*, Vol. 24, No. 2, pp. 1773-1780, (2016).
- [39] I. S. Amiri, M. M. Ariannejad, V. Kouhdaragh, S. A. Seyedi, and P. Yupapin, "Microring resonator made by ion-exchange technique for detecting the CO<sub>2</sub>, H<sub>2</sub>O, NaCl as cladding layer", *Journal of King Saud University-Science*, Vol. 31, No. 1, pp. 27-32, (2019).
- [40] K. P. Koushik and S. Malathi, "Optical micro-ring resonator for detection of carbon dioxide gas", In *Emerging Trends in Photonics, Signal Processing, and Communication Engineering*, pp. 157-161, (2020).
- [41] D. G. Rabus and C. Sada, "Integrated Ring Resonators", *Springer Series in Optical Sciences*, Vol. 127 (2020).

- [42] W. Bogaerts, P. De Heyn, T. Van Vaerenbergh, K. De Vos, S. Kumar Selvaraja, T. Claes, P. Dumon, P. Bienstman, D. Van Thourhout and R. Baets, "Silicon microring resonators", *Laser & Photonics Reviews*, Vol. 6, No. 1, pp. 47-73, (2012).
- [43] Y. S. Yi, D. C. Wu, P. Birar and Z. Yang, "Ring resonator-based optical hydrogen sensor", *IEEE Sens. J.*, Vol. 17, No. 7, pp. 2042-2047 (2017).
- [44] G. N. Tsigaridas, "A study on refractive index sensors based on optical micro-ring resonators", *Photonic Sensors*, Vol. 7, No. 3, pp. 217-225 (2017).
- [45] H. H. Li, "Refractive index of silicon and germanium and its wavelength and temperature derivatives", *Journal of Physical and Chemical Reference Data*, Vol. 9, No. 3, pp. 561-658 (1980).
- [46] I. H. Malitson, "Interspecimen comparison of the refractive index of fused silica", *Josa*, Vol. 55, No. 10, pp. 1205-1209 (1965).
- [47] E. A. Tikhonov, A. K. Lyamets and Y. V. Malyukin, "Refractive index of nanoscale thickness films measured by Brewster refractometry," arXiv preprint arXiv: 1504.04262, (2015).
- [48] Y. Dektyar and P. Shipkovs, "Cylindrical cell-based refractometer and the methodology of its application", Ph.D. thesis, Riga Technical University, (2015).
- [49] S. J. Clark, M. D. Segall, C. J. Pickard, P. J. Hasnip, M. J. Probert, K. Refson and M. C. Payne, "Materials Studio", CASTEP, version 5.0, San Diego, CA: Accelrys, (2009).
- [50] D. R. Hamann, M. Schlüter and C. Chiang, "Norm-conserving pseudopotentials", *Phys. Rev. Lett.*, Vol. 43, No. 20, pp. 1494-1497 (1979).
- [51] M. Dolatyari, A. Rostami, S. Mathur, and A. Klein, "Trap engineering in solution-processed PbSe quantum dots for high-speed MID-infrared photodetectors", *J. Mater. Chem. C*, Vol. 7, No. 19, pp. 5658-5669 (2019).